

The joint detection rate of short gamma-ray bursts and gravitational waves from binary neutron star mergers

Chong-Yu Gao,^{1,2} Jun-Jie Wei^{1,2}* and Hou-Dun Zeng^{1,3}

¹Purple Mountain Observatory, Chinese Academy of Sciences, Nanjing 210023, China

²School of Astronomy and Space Sciences, University of Science and Technology of China, Hefei 230026, China

³Key Laboratory of Dark Matter and Space Astronomy Purple Mountain Observatory, Chinese Academy of Sciences Nanjing, 210023, China

Accepted XXX. Received YYY; in original form ZZZ

ABSTRACT

In this work, we analyze the most recent short gamma-ray burst (sGRB) sample detected by the *Fermi* satellite to reassess the sGRB luminosity function and formation rate. Using the empirical luminosity correlation, we first determine the pseudo redshifts of 478 sGRBs. Then, we use the maximum likelihood method to constrain the luminosity function and formation rate of sGRBs under various delay-time distribution models, finding the power-law delay model marginally preferred over the Gaussian and lognormal delay models based on the Akaike Information Criterion. The local formation rate of sGRBs is $1.73^{+0.60}_{-0.45} \text{ Gpc}^{-3} \text{ yr}^{-1}$, largely independent of the adopted delay-time distribution model. Additionally, we investigate the potential for joint detection of sGRBs and their gravitational wave (GW) counterparts from binary neutron star mergers using both current and future GRB and GW facilities. For sGRB detection, we consider three existing satellites: *Fermi*, the Space-based multi-band astronomical Variable Objects Monitor (*SVOM*), and the Einstein Probe (*EP*). For GW detection, we examine two International GW Networks (IGWN): a four-detector network consisting of LIGO Hanford, Livingston, Virgo, and Kagra (IGWN4) and an upcoming five-detector network that includes these four detectors plus LIGO India (IGWN5). Our results indicate that for different delay-time distribution models, the joint sGRB and GW detection rates for *Fermi*, *SVOM*, and *EP* with IGWN4 (IGWN5) lie within $0.09\text{--}0.31 \text{ yr}^{-1}$ ($0.55\text{--}1.98 \text{ yr}^{-1}$), $0.03\text{--}0.11 \text{ yr}^{-1}$ ($0.26\text{--}0.80 \text{ yr}^{-1}$), and $0.01\text{--}0.04 \text{ yr}^{-1}$ ($0.09\text{--}0.27 \text{ yr}^{-1}$), respectively.

Key words: gamma-ray bursts – gravitational waves – neutron star mergers – methods: statistical

1 INTRODUCTION

Gamma-ray bursts (GRBs) are the most energetic explosions in the Universe. They are typically divided into two groups based on a critical duration value of $T_{90} = 2$ seconds (Kouveliotou et al. 1993). Long GRBs are generally believed to originate from the core collapses of massive stars (Woosley 1993), whereas short GRBs (sGRBs) are thought to result from the mergers of two compact objects, such as neutron stars (NSs) or black holes (BHs) (Eichler et al. 1989). The multimessenger observations of the gravitational wave event (GW170817) and its associated sGRB (GRB 170817A) from a binary neutron star (BNS) merger have provided compelling evidence supporting the compact star merger origin of sGRBs (Abbott et al. 2017; Goldstein et al. 2017; Savchenko et al. 2017). Moreover, the abundant multiwavelength follow-up observations of the afterglow of GRB 170817A also spurred extensive research into the jet structure and the radiation processes of sGRBs (Troja et al. 2017; Lyman et al. 2018; Margutti et al. 2018; Mooley et al. 2018a,b; Troja et al. 2018; Ghirlanda et al. 2019; Beniamini et al. 2020a,b; Troja et al. 2020).

The multimessenger joint observations of gravitational waves (GWs) and sGRBs provide valuable information about the jet launching time and the propagation of the jet through the ejecta. Therefore, these observations are an ideal probe to understand not only the

sGRB sources but also the jet dynamics and the emission mechanism (Nakar 2007; Berger 2014; Nakar 2020). However, aside from GW170817/GRB 170817A, no other joint GW and sGRB detections have been identified, which hinders the advancement of our understanding of the sGRB origins and the jet mechanism.

The formation rate of sGRBs is directly related to the expected number of GW events associated with sGRBs for the current and upcoming high-energy GRB and GW facilities. However, the number of sGRBs with redshift measurements is very small, making it difficult to estimate the sGRB formation rate. Due to the small sample size, previous studies estimated the local sGRB formation rate to range from $0.1 \text{ Gpc}^{-3} \text{ yr}^{-1}$ to $400 \text{ Gpc}^{-3} \text{ yr}^{-1}$ (Guetta & Piran 2005, 2006; Nakar et al. 2006a; Guetta & Stella 2009; Dietz 2011; Petrillo et al. 2013; Siellez et al. 2014; Sun et al. 2015; Ghirlanda et al. 2016; Liu & Yu 2019; Dainotti et al. 2021; Dimitrova et al. 2023). Using the empirical correlation between the spectral peak energy E_p and the peak luminosity L (Yonetoku et al. 2004; Tsutsui et al. 2013), Yonetoku et al. (2014) determined the pseudo redshifts of those sGRBs without a known redshift, thereby enlarging the available sGRB sample. Then they derived the luminosity function (LF) and formation rate of sGRBs by using the non-parametric Lynden-Bell c^- method (see also Zhang & Wang 2018). Keep in mind that the Lynden-Bell c^- method necessitates a certain uniformity in data coverage to be applicable (Lynden-Bell 1971). In reality, however, sGRB data suffer from the truncation of the flux limit of the detector, and the detector's

* E-mail: jjwei@pmo.ac.cn

sensitivity is hard to parametrize, making it challenging to construct a uniformly distributed sample of sGRBs. Maximum-likelihood algorithms (Marshall et al. 1983) are preferable for addressing the sGRB problem because they are less constrained by the conditions of a given sample and offer greater flexibility in modeling systematic uncertainties. In this study, we follow the treatment of Yonetoku et al. (2014) and Zhang & Wang (2018) to first obtain the pseudo redshifts of sGRBs observed by *Fermi* using the E_p - L correlation. To account for systematics and unknowns in our statistical analysis, we then employ the maximum likelihood method to examine the enlarged sGRB sample, thereby constraining the LF and formation rate of sGRBs.

With the derived LF and formation rate of sGRBs, we can further investigate the joint detection prospects of sGRBs and their GW counterparts using GRB and GW facilities. The success of joint GW and sGRB detections depends on the sensitivities and capabilities of both GW detectors and GRB missions. Currently, the fourth observation (O4) run of the International Gravitational Wave Network-4 (IGWN4), which includes four detectors—Advanced LIGO Livingston and Hanford (LIGO Scientific Collaboration et al. 2015), Advanced Virgo (Acernese et al. 2015), and Kagra at design sensitivity (Aso et al. 2013)—is ongoing. In the future, the LIGO detectors at Livingston and Hanford will be upgraded to A+ sensitivity (Barsotti et al. 2018), and the planned GW detector LIGO-India (Iyer et al. 2011; Saleem et al. 2022) will join the detector network, forming the International Gravitational Wave Network-5 (IGWN5). This IGWN5 network will significantly enhance the GW detection capabilities of its detectors. As the sensitivity and detection horizon of GW detectors continue to improve significantly, the primary limitation for joint detections is likely to soon be the sensitivity of GRB detectors such as *Fermi*. Recently, the Space-based multi-band astronomical Variable Objects Monitor (*SVOM*; Atteia et al. 2022) and the Einstein Probe (*EP*; Yuan et al. 2022) have been launched into space. Both satellites share the important scientific objective of detecting the electromagnetic counterparts of GWs. Estimating the expected detection rates of sGRB associated with GWs for these two missions will be crucial for subsequent observational plans and related research.

In this work, we analyze the most recent sGRB sample detected by *Fermi*'s Gamma-ray Burst Monitor (*Fermi*/GBM) to determine the LF and formation rate of sGRBs through the application of the maximum likelihood method. Then, we explore the potential for joint sGRB and GW detections from BNS mergers using existing and upcoming GRB and GW facilities. For sGRB detection, we consider three existing satellites: *Fermi*, *SVOM*, and *EP*. For GW detection, we consider two GW detector networks: the current IGWN4 and the upcoming IGWN5. Discussions have been held regarding sGRB-like emissions from NS-BH mergers; however, the theoretical aspects remain unclear, and there is currently no observational confirmation. Therefore, we exclude NS-BH mergers from our analysis.

This paper is organized as follows. In Section 2, we describe the *Fermi*/GBM sample available to us, and obtain the pseudo redshifts of sGRBs. In Section 3, the LF and formation rate of sGRBs are determined through the maximum likelihood method. The synthetic BNS population model, the sGRB detection rates, and the prospects of joint sGRB and GW detections are presented in Section 4. Finally, we provide a brief summary and discussion in Section 5. Throughout this paper, we assume a standard Λ CDM cosmological model and adopt the parameters of $H_0 = 69.32 \text{ km s}^{-1} \text{ Mpc}^{-1}$, $\Omega_m = 0.2865$, and $\Omega_\Lambda = 0.7135$ (Hinshaw et al. 2013).

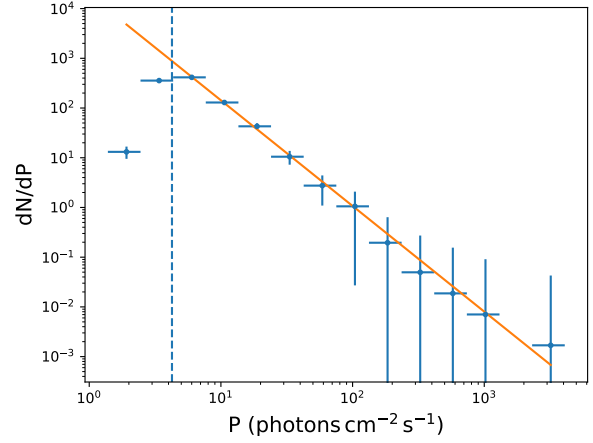


Figure 1. The peak-flux distribution of 553 sGRBs detected by *Fermi*/GBM. The vertical dashed line stands for the limiting flux ($\sim 4.1 \text{ photons cm}^{-2} \text{ s}^{-1}$) above which the instrumental selection effect on incomplete sampling of faint bursts becomes negligible. The solid line represents the best power-law fit to the peak-flux distribution for $P \geq 4.1 \text{ photons cm}^{-2} \text{ s}^{-1}$.

2 FERMI GRB SAMPLE AND REDSHIFT ESTIMATION

2.1 Sample selection

Since the launch of the *Fermi* satellite on 2008 June, 3671 GRBs have been detected up to 2023 December 15. We select 553 sGRBs with durations $T_{90} < 2 \text{ s}$ in the observer frame. For each sGRB, we download the 64 ms peak photon flux P (in units of $\text{photons cm}^{-2} \text{ s}^{-1}$) in the 10–1000 keV energy band and the spectral parameters (including the low- and high-energy photon indices α and β , and the observed peak energy E_p) from the online *Fermi*/GBM burst catalog (Gruber et al. 2014; von Kienlin et al. 2014; Narayana Bhat et al. 2016; von Kienlin et al. 2020).¹ Figure 1 shows the peak-flux distribution of all the 553 sGRBs, ranging from 1.91 to 3198.53 $\text{photons cm}^{-2} \text{ s}^{-1}$. In practice, not all faint GRBs with peak flux slightly above the *Fermi*/GBM threshold are successfully triggered. As shown in Figure 1, because of incomplete sampling of faint bursts, the peak-flux distribution obviously deviates from an ideal power law at the low end. To avoid complications arising from a detailed treatment of the *Fermi*/GBM trigger, we focus on a sample of 512 sGRBs with peak flux $P \approx 4.1 \text{ photons cm}^{-2} \text{ s}^{-1}$ and above. Indeed, above the flux limit ($P_{\text{lim}} = 4.1 \text{ photons cm}^{-2} \text{ s}^{-1}$), the instrumental selection effect on incomplete sampling is negligible (see Figure 1). Thus, we assume that the trigger efficiency of bursts with $P \geq P_{\text{lim}}$ is 100%.

2.2 Redshift estimation for sGRBs

The current number of sGRBs with redshift measurements is very small. In order to study their LF and formation rate, we determine the pseudo redshifts of sGRBs observed by *Fermi*/GBM using the empirical correlation between E_p and the peak bolometric luminosity L (Tsutsui et al. 2013; Zhang & Wang 2018). This correlation is given by (Zhang & Wang 2018)

$$L = (7.15 \pm 0.49) \times 10^{50} \left[\frac{E_p (1+z)}{100 \text{ keV}} \right]^{1.63 \pm 0.03}, \quad (1)$$

¹ <https://heasarc.gsfc.nasa.gov/W3Browse/fermi/fermigbrst.html>

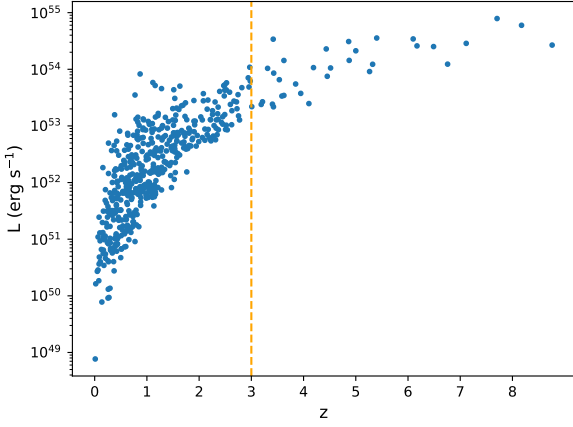


Figure 2. Pseudo redshift–luminosity distribution of 512 *Fermi* sGRBs estimated by the E_p – L correlation. The vertical dashed line represents the truncated redshift of $z = 3$, below which 478 bursts are used for our analysis.

which can be rewritten as

$$\frac{d_l^2(z)}{(1+z)^{1.63}} = \frac{7.15 \times 10^{50}}{4\pi F_p} \left(\frac{E_p}{100 \text{ keV}} \right)^{1.63}, \quad (2)$$

where d_l is the luminosity distance and F_p is the bolometric peak flux at 64 ms time intervals (in units of $\text{erg cm}^{-2} \text{s}^{-1}$). The pseudo redshift of each burst can be estimated using the spectral parameters of the Band function (Band et al. 1993) and the 64 ms peak photon flux P . With the pseudo redshift, we can further calculate the peak bolometric luminosity L in the 1 – 10^5 keV rest-frame energy range. In our calculations, we adopt the spectral parameters from the *Fermi*/GBM burst catalog. For items that lack records, the low- and high-energy photon spectral indices are set to $\alpha = -1$ and $\beta = -2.25$ (Preece et al. 2000; Kaneko et al. 2006), and E_p is randomly selected from the observed values. The pseudo redshift–luminosity distribution of 512 sGRBs is shown in Figure 2. Since the maximum redshift observed for sGRBs is 2.609, we exclude those bursts with pseudo-redshifts $z > 3$. Hereafter, we use 478 sGRBs with $P \geq 4.1$ photons $\text{cm}^{-2} \text{s}^{-1}$ and $z \leq 3$ for further analysis.

3 SGRB LUMINOSITY FUNCTION AND FORMATION RATE

3.1 Analysis method

In this work, we use the maximum likelihood method proposed by Marshall et al. (1983) to constrain the sGRB LF and redshift distribution. The likelihood function is defined as (e.g., Chiang & Mukherjee 1998; Narumoto & Totani 2006; Ajello et al. 2009, 2012; Abdo et al. 2010; Lan et al. 2019, 2021, 2022)

$$\mathcal{L} = \exp(-N_{\text{exp}}) \prod_{i=1}^{N_{\text{obs}}} \Phi(L_i, z_i, t_i), \quad (3)$$

where N_{exp} is the expected number of sGRB detections, N_{obs} is the observed number of the sample, and $\Phi(L, z, t)$ denotes the observed rate of sGRBs per unit time at redshift $z \sim z + dz$ with luminosity $L \sim L + dL$, which can be written as

$$\Phi(L, z, t) = \frac{d^3 N}{dt dL dz} = f_{\text{sky}} f_{\text{not_SAA}} \frac{R_{\text{sGRB}}(z)}{1+z} \frac{dV(z)}{dz} \phi(L), \quad (4)$$

where $f_{\text{sky}} = 0.7$ is the sky-coverage fraction of *Fermi*/GBM,² $f_{\text{not_SAA}} = 0.85$ denotes the fraction of *Fermi*'s orbit outside the South Atlantic Anomaly (SAA), $R_{\text{sGRB}}(z)$ is the comoving rate density of sGRBs in units of $\text{Mpc}^{-3} \text{yr}^{-1}$, the factor $(1+z)^{-1}$ reflects the cosmological time dilation, $\phi(L)$ is the normalized LF of sGRBs, and $dV(z)/dz = 4\pi c d_l^2(z)/[H_0(1+z)^2 \sqrt{\Omega_m(1+z)^3 + \Omega_\Lambda}]$ is the comoving volume element in a flat Λ CDM cosmology.

It is believed that sGRBs originate from the mergers of two compact stars, either NS-NS or NS-BH. A compact binary system undergoes a long inspiral phase before the final merger, resulting in a significant time delay with respect to star formation (Faber & Rasio 2012; Burns 2020). If we assume that the fraction of mass forming compact binary systems relative to the total mass forming newborn stars remains constant over cosmological time, then the sGRB rate density $R_{\text{sGRB}}(z)$ can be represented as a convolution of the star formation rate density (SFRD) $\psi_\star(z)$ and the probability density function of the delay time distribution $P(\tau)$ (Paul 2018; Liu & Yu 2019; Luo et al. 2022):

$$R_{\text{sGRB}}(z) = f_b C \int_{\tau_{\text{min}}}^{\tau_{\text{max}}} \psi_\star[z'(\tau)] P(\tau) d\tau, \quad (5)$$

where f_b represents the beaming factor of the relativistic jets responsible for the burst, and C is the sGRB formation efficiency per unit available mass (in units of M_\odot^{-1}). In the maximum likelihood analysis, the parameters C and f_b are degenerate. That is, one can vary either C or f_b , but not both. Therefore, we adopt a definition

$$\eta \equiv f_b C, \quad (6)$$

where η is the ‘ f_b -free’ formation efficiency, still in units of M_\odot^{-1} . Here, $z'(\tau)$ denotes the redshift at the formation of the compact binary system, while z corresponds to the redshift of the sGRB event. Thus, the delay time between the formation and merger of the compact binary system is given by $\tau = t(z) - t(z')$, where $t(z)$ and $t(z')$ are the ages of the Universe at redshifts z and z' , respectively. In view of the fact that the progenitors of NSs usually have initial masses of 10 – 29 M_\odot , and their lifetimes are 10 – 30 Myr , we set the minimum delay time to be $\tau_{\text{min}} = 10 \text{ Myr}$, as done by Luo et al. (2022) in their treatment. The age of the Universe at redshift z , $t(z)$, is set as the maximum delay time τ_{max} . The SFRD $\psi_\star(z)$ can be expressed approximately by the analytical form (Yüksel et al. 2008):

$$\psi_\star(z) = \rho_0 \left[(1+z)^{3.4\omega} + \left(\frac{1+z}{5000} \right)^{-0.3\omega} + \left(\frac{1+z}{9} \right)^{-3.5\omega} \right]^{1/\omega}, \quad (7)$$

where $\rho_0 = 0.02 \text{ M}_\odot \text{yr}^{-1} \text{Mpc}^{-3}$ is the local SFRD, and $\omega = -10$.

For the delay time distribution $P(\tau)$, we consider three most widely discussed models: Gaussian, Lognormal, and Power law, whose functional forms can be expressed as:

(i) Gaussian (Virgili et al. 2011):

$$P(\tau) \propto \frac{1}{\sqrt{2\pi}\sigma_G} \exp \left[-\frac{(\tau - t_G)^2}{2\sigma_G^2} \right], \quad (8)$$

where t_G and σ_G represent, respectively, the mean and the standard deviation of τ .

² *Fermi* is a low earth-orbit satellite that suffers from limited sky coverage because the Earth blocks $\sim 30\%$ of the sky.

(ii) Lognormal (Wanderman & Piran 2015):

$$P(\tau) \propto \frac{1}{\sqrt{2\pi}\tau\sigma_{\text{LN}}} \exp\left[-\frac{(\ln \tau - \ln t_{\text{LN}})^2}{2\sigma_{\text{LN}}^2}\right], \quad (9)$$

where $\ln t_{\text{LN}}$ and σ_{LN} represent, respectively, the mean and the standard deviation of $\ln \tau$.

(iii) Power law (Nakar et al. 2006b):

$$P(\tau) \propto \tau^{-\gamma}, \quad (10)$$

where γ is the power-law index.

For the sGRB LF $\phi(L)$, we adopt the widely recognized expression in terms of a broken power law:

$$\phi(L) \propto \begin{cases} \left(\frac{L}{L_b}\right)^{-\nu_1}; & L \leq L_b, \\ \left(\frac{L}{L_b}\right)^{-\nu_2}; & L > L_b, \end{cases} \quad (11)$$

where ν_1 and ν_2 are the power-law indices before and after the break luminosity L_b . The normalization constant of the LF is calculated between the minimum and maximum luminosities, $L_{\text{min}} = 10^{49}$ erg s^{-1} and $L_{\text{max}} = 10^{55}$ erg s^{-1} (Tan et al. 2018).

Finally, when considering *Fermi*/GBM having a flux threshold of $P_{\text{lim}} = 4.1$ photons $\text{cm}^{-2} \text{s}^{-1}$ in the 10–1000 keV energy band, the expected number of sGRBs should be

$$N_{\text{exp}} = T f_{\text{sky}} f_{\text{not_SAA}} \int_0^{z_{\text{max}}} \frac{R_{\text{sGRB}}(z)}{1+z} \frac{dV(z)}{dz} dz \int_{\max[L_{\text{min}}, L_{\text{lim}}(z)]}^{L_{\text{max}}} \phi(L) dL, \quad (12)$$

where $T \sim 15.5$ yr is the observational period of *Fermi* that covers our sample, and $z_{\text{max}} = 3$ corresponds to the maximum redshift of our sample. For a given redshift z , the luminosity threshold can be determined by

$$L_{\text{lim}}(z) = 4\pi d_L^2(z) P_{\text{lim}} k(z), \quad (13)$$

where $k(z)$ is the spectral k -correction factor converting *Fermi*/GBM's observed energy band of 10–1000 keV (denoted by $E_{\text{min}}-E_{\text{max}}$ keV) into the rest-frame band of 1–10⁵ keV. For *Fermi* bursts, the flux threshold P_{lim} is given in units of photons $\text{cm}^{-2} \text{s}^{-1}$, hence

$$k(z) = \frac{\int_{1/(1+z)}^{10^5/(1+z)} EN(E) dE}{\int_{E_{\text{min}}}^{E_{\text{max}}} N(E) dE}, \quad (14)$$

where $N(E)$ is the observed photon spectrum. While for other detectors with P_{lim} given in erg $\text{cm}^{-2} \text{s}^{-1}$, the k -correction factor should be rewritten as follows:

$$k(z) = \frac{\int_{1/(1+z)}^{10^5/(1+z)} EN(E) dE}{\int_{E_{\text{min}}}^{E_{\text{max}}} EN(E) dE}. \quad (15)$$

To describe $N(E)$, we adopt a typical Band spectrum, characterized by photon spectral indices of $\alpha = -1$ and $\beta = -2.25$ (Band et al. 1993; Preece et al. 2000; Kaneko et al. 2006). For a given L , the spectral peak energy E_p is estimated through the empirical $E_p - L$ correlation (i.e., Equation 1).

3.2 Results

For a given delay-time distribution model, we optimize the free parameters by maximizing the likelihood function (Equation 3). The

delay time distribution $P(\tau)$ has one or two free parameters (e.g., t_G and σ_G for Gaussian delay, t_{LN} and σ_{LN} for lognormal delay, or γ for power-law delay). The sGRB LF $\phi(L)$ has three free parameters (ν_1 , ν_2 , and L_b). Additionally, the sGRB rate density $R_{\text{sGRB}}(z)$, given by Equation (5), depends on the sGRB formation efficiency η , resulting in a total of five or six free parameters. For each model, the Python Markov chain Monte Carlo (MCMC) module, EMCEE (Foreman-Mackey et al. 2013), is employed to derive multidimensional parameter constraints from the observational data.

Table 1 lists the best-fitting parameters and their corresponding 1σ uncertainties for different models. In the last two columns, we also list the log likelihood value ($\ln \mathcal{L}$) and the Akaike Information Criterion (AIC) score, which can be used to statistically judge which of the models is preferred by the observational data. For each model, the AIC score is calculated as $\text{AIC} = -2 \ln \mathcal{L} + 2n$, where n is the number of free parameters (Akaike 1974; Liddle 2007). Given multiple different models $\mathcal{M}_1, \mathcal{M}_2, \dots, \mathcal{M}_N$, each with the corresponding AIC scores $\text{AIC}_1, \text{AIC}_2, \dots, \text{AIC}_N$, the unnormalized confidence that model \mathcal{M}_i is correct is the Akaike weight $\exp(-\text{AIC}_i/2)$. Thus, the relative probability that \mathcal{M}_i is statistically preferred is

$$P(\mathcal{M}_i) = \frac{\exp(-\text{AIC}_i/2)}{\exp(-\text{AIC}_1/2) + \dots + \exp(-\text{AIC}_N/2)}. \quad (16)$$

Figure 3 presents the redshift and luminosity distributions of 478 sGRBs with $P \geq 4.1$ photons $\text{cm}^{-2} \text{s}^{-1}$ and $z \leq 3$. To facilitate a direct comparison among different delay-time distribution models, we show in Figure 3 the best-fitting theoretical curves for the power-law delay model (orange solid), the Gaussian delay model (black dashed), and the lognormal delay model (purple dot-dashed). One can see from this plot that the expectations from these three models appear to fit the observed z and L distributions comparably well. According to the AIC model selection criterion, we find that the power-law delay model is preferred with an approximate relative probability of 72%, while the lognormal and Gaussian delay models are somewhat less favored, with relative probabilities of approximately 26% and 1%, respectively.

With the best-fitting parameters presented in Table 1, we are able to calculate the local sGRB formation rate at $z = 0$ ($R_{\text{sGRB}}(0)$) using Equation (5). We find $R_{\text{sGRB}}(0) = 1.73_{-0.45}^{+0.60}$ Gpc⁻³ yr⁻¹ for the power-law delay model, $1.57_{-0.78}^{+0.76}$ Gpc⁻³ yr⁻¹ for the Gaussian delay model, and $1.31_{-0.61}^{+0.85}$ Gpc⁻³ yr⁻¹ for the lognormal delay model, which are consistent with each other within the 1σ confidence level. We would like to stress that our derived local sGRB formation rate is broadly consistent with previous results (Guetta & Piran 2005; Yonetoku et al. 2014; Ghirlanda et al. 2016; Paul 2018).

4 JOINT GW AND SGRB DETECTION

In this section, we will first describe the synthetic BNS population and provide estimates of the GW detection rates by the GW detector networks. Next, we will calculate the sGRB detection rates for high-energy satellites. Finally, we will study the joint detection prospects of GWs and their sGRB counterparts from BNS mergers.

4.1 GW detection rate simulation

Following Bhattacharjee et al. (2024), we inject $N_{\text{inj}} = 300,000$ sources from BNS mergers up to a luminosity distance of $d_L = 1.6$ Gpc (corresponding to a comoving distance of ~ 1.2 Gpc and a redshift of $z \sim 0.3$). The number of injected sources is oversampled by a factor of ~ 130 from the merger rate of BNSs (median rate

Table 1. Best-fitting parameters for different delay-time distribution models.

Delay model	Delay parameter	$\log_{10} \eta$ (M_{\odot}^{-1})	$\log_{10} L_b$ (erg s^{-1})	ν_1	ν_2	$\ln \mathcal{L}$	AIC
Gaussian	$t_G = 1.08^{+0.71}_{-0.64}$, $\sigma_G = 0.40^{+0.39}_{-0.34}$	$1.28^{+0.15}_{-0.13}$	$51.83^{+0.28}_{-0.16}$	$1.20^{+0.10}_{-0.09}$	$1.63^{+0.07}_{-0.05}$	-47473	94958
Lognormal	$t_{\text{LN}} = 1.10^{+0.74}_{-0.71}$, $\sigma_{\text{LN}} = 0.22^{+0.17}_{-0.14}$	$1.22^{+0.15}_{-0.16}$	$51.32^{+0.57}_{-0.40}$	$1.20^{+0.19}_{-0.10}$	$1.56^{+0.07}_{-0.05}$	-47470	94952
Power law	$\gamma = 1.40^{+0.34}_{-0.31}$	$1.45^{+0.12}_{-0.12}$	$52.04^{+0.27}_{-1.05}$	$1.22^{+0.13}_{-0.13}$	$1.64^{+0.19}_{-0.06}$	-47470	94950

Note. t_G , t_{LN} , and σ_G are in units of Gyr, and σ_{LN} is in units of ln Gyr.

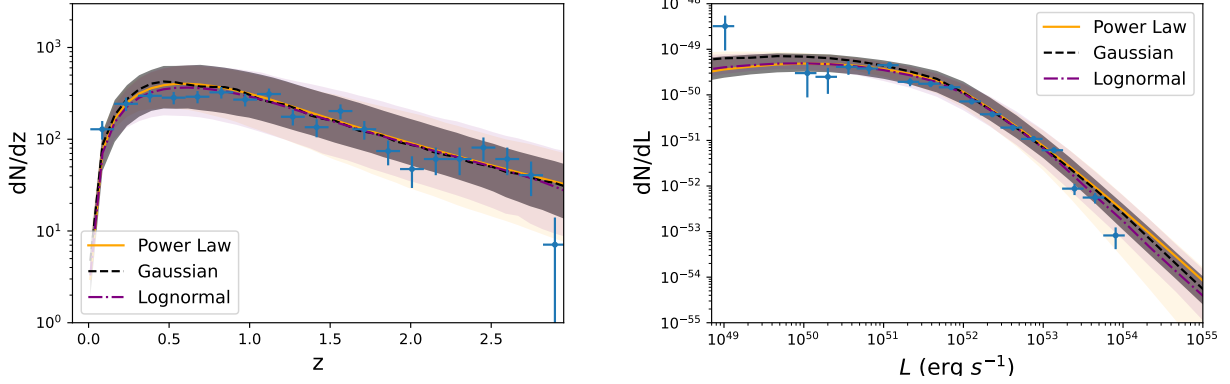


Figure 3. Redshift and luminosity distributions of 478 *Fermi* sGRBs with $P \geq 4.1$ photons $\text{cm}^{-2} \text{s}^{-1}$ and $z \leq 3$ (the blue points, with the detection number in each redshift or luminosity bin, are indicated by a solid point with Poisson error bars). Different curves correspond to the expected distributions from various best-fitting delay time distribution models: power-law delay (orange solid lines), Gaussian delay (black dashed lines), and lognormal delay (purple dot-dashed lines). Shaded areas show the 1σ confidence regions of the corresponding models.

~ 2316 , Abbott et al. 2021a,b) within the same comoving volume. This oversampling is conducted to avoid any effects of small number statistic on our results. The injected sources are uniformly distributed in the rest-frame comoving volume, which translates to a redshift probability distribution of

$$\frac{dp(z)}{dz} \propto \frac{1}{1+z} \frac{dV(z)}{dz}. \quad (17)$$

We assume that the mass distribution of the neutron stars obeys a normal distribution with a mean of $1.33 M_{\odot}$ and a standard deviation of $0.09 M_{\odot}$ (Özel & Freire 2016). The spins of the neutron stars are uniformly distributed between $0 < \chi < 0.05$, with the upper limit set by the maximum known neutron star spin (Zhu et al. 2018). The direction of the orbital angular momentum is uniformly distributed in space. We generate the GW waveforms using the Python package PyCBC³ with the IMPRPhenomPv2 approximant model (Schmidt et al. 2012; Hannam et al. 2014; Khan et al. 2016).

To determine which injected BNS merger events can be detected by two different GW detection networks, IGWN4 and IGWN5, we consider those events above a particular threshold value of the network signal-to-noise ratio, i.e.,

$$\text{SNR}_{\text{net}} = \sqrt{\sum_{\text{det}} \text{SNR}_{\text{det}}^2}, \quad (18)$$

where SNR_{det} is the signal-to-noise ratio (SNR) of a single detector (Pai et al. 2001). In this work, we define the criterion of $\text{SNR}_{\text{net}} > 8$

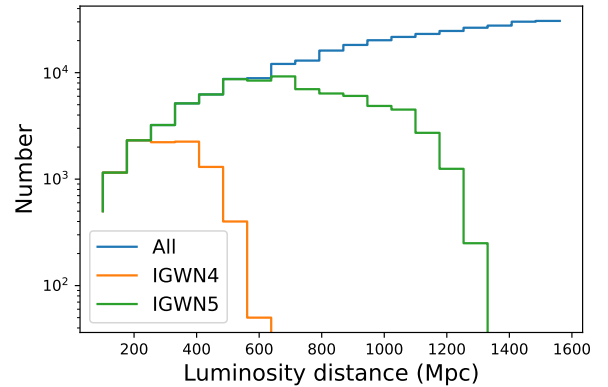


Figure 4. The distribution of the injected BNS merger events over luminosity distance (blue histogram). The yellow and green histograms correspond to the distributions of events detected above the threshold SNR_{net} of 8 by IGWN4 and IGWN5, respectively.

as the detection threshold (Petrov et al. 2022). For a given single detector, the SNR_{det} could be calculated by (Babak et al. 2021)

$$\text{SNR}_{\text{det}}^2 = 4 \text{Re} \left(\int_{f_{\text{min}}}^{f_{\text{max}}} df \frac{\tilde{X} \tilde{X}^*}{S_n(f)} \right), \quad (19)$$

where \tilde{X} represents the complex GW signal, and $S_n(f)$ is the noise

³ <https://pycbc.org/>

power spectral density of the corresponding detector, which can be downloaded from the Sensitive Curves website⁴.

From the above simulation, we obtain the distribution of the injected BNS merger events over luminosity distance, which is presented in Figure 4 as the blue histogram. In this plot, we also show the distribution of the events detected above the threshold SNR_{net} of 8 by either IGWN4 (yellow histogram) or IGWN5 (green histogram). From Figure 4, one can calculate the GW detection rate ($R_{\text{GW}}(z)$) as a function of redshift (or luminosity distance) simply by dividing the number of detections by IGWN4 (IGWN5) by the number of all injected events at different redshifts.

4.2 sGRB detection rates

To determine the prospects of sGRB detection, we consider three existing high-energy GRB detectors: *Fermi*/GBM (10–1000 keV), the Gamma-Ray Monitor (GRM) of *SVOM* (1–1000 keV), and the Wide-field X-ray Telescope (WXT) of *EP* (0.5–4 keV). The energy bands, flux thresholds, sky-coverage fractions, and SAA-outage fractions of these three high-energy emissions are summarized in Table 2.

With the flux threshold and the effective detection fraction of each detector, we compute the sGRB detection rate up to a luminosity distance of $d_L = 1.6$ Gpc (corresponding to $z = 0.3$, the same distance limit as the BNS merger events), fixing the model-free parameters to the values given in Table 1. For the power-law delay model, our results show that the sGRB detection rate is $3.69^{+2.25}_{-1.55} \text{ yr}^{-1}$ for *Fermi*/GBM, $1.96^{+0.88}_{-0.60} \text{ yr}^{-1}$ for *SVOM*/GRM, and $0.57^{+0.27}_{-0.18} \text{ yr}^{-1}$ for *EP*/WXT. For the same detector, similar sGRB detection rates are derived for different delay-time distribution models. The derived sGRB detection rates for the high-energy GRB detectors are listed in Columns 2–4 of Table 3. It is clear that *Fermi*/GBM has the highest sGRB detection rate. Due to their relatively low sky coverage, the other two detectors, *SVOM*/GRM and *EP*/WXT, have lower detection rates, in that order.

It should be underlined that our analysis is limited by the distance cut-off of $d_L = 1.6$ Gpc ($z = 0.3$). Thus, events beyond this distance limit are missed by our calculations. However, in reality, many higher-redshift ($z > 0.3$) events will be detected by high-energy GRB missions. This makes the sGRB detection rates calculated here lower than the true sGRB detection rates by these missions.

4.3 Joint sGRB and GW detection rates

By combining the GW detection rate ($R_{\text{GW}}(z)$) with the observed sGRB distributions, the expected number of joint sGRB and GW detections from BNS mergers can be estimated using specific GRB and GW facilities through the following equation:

$$N_{\text{joint}} = T f_{\text{sky}} f_{\text{not_SAA}} \int_0^{z_{\text{lim}}} \frac{R_{\text{sGRB}}(z) R_{\text{GW}}(z) dV(z)}{1+z} \frac{dV(z)}{dz} dz \int_{\max[L_{\text{min}}, L_{\text{lim}}(z)]}^{L_{\text{max}}} \phi(L) dL, \quad (20)$$

where $z_{\text{lim}} = 0.3$ (corresponding to 1.6 Gpc) is the distance limit of this work. Again, in our calculations, the model-free parameters are fixed at the best-fitting values given in Table 1.

For the sensitivity of the IGWN4, the overall joint sGRB and GW

detection rates are rather low. The joint detection rates for the high-energy GRB detectors *Fermi*/GBM, *SVOM*/GRM, and *EP*/WXT lie in the range of 0.09–0.31, 0.03–0.11, and 0.01–0.04 yr^{-1} , respectively, for different delay-time distribution models (see Columns 5–7 of Table 3). The joint detection rate expected from *Fermi*/GBM and IGWN4 means that only 1–3 sGRB and GW associated events would be detected in about 10 years of observation, which is consistent with the current result that only one joint detection of GW170817/GRB 170817A has been found. After the GW detection network is upgraded to IGWN5, the joint detection rates increase to 0.55–1.98, 0.26–0.80, and 0.09–0.27 yr^{-1} for *Fermi*/GBM, *SVOM*/GRM, and *EP*/WXT, respectively (see Columns 8–10 of Table 3).

5 CONCLUSIONS AND DISCUSSION

In this paper, we have updated and expanded the sGRB sample detected by the *Fermi* satellite, which now includes 553 sGRBs as of December 2023. Due to instrumental limitations in sampling faint bursts, we focused on sGRBs that are sufficiently bright in the 10–1000 keV *Fermi*/GBM energy band. Specifically, we selected bursts with a 64-ms peak photon flux of $P \geq 4.1$ photons $\text{cm}^{-2} \text{ s}^{-1}$. Above this flux threshold, the incomplete flux sampling due to instrumental selection effects becomes negligible. Consequently, our subsample consists of 512 sGRBs with $P \geq 4.1$ photons $\text{cm}^{-2} \text{ s}^{-1}$. Given the limited number of sGRBs with known redshifts, we estimated the pseudo redshifts of 512 sGRBs using the empirical E_p - L correlation. Since the maximum redshift observed for sGRBs is 2.609, we excluded those bursts with pseudo-redshifts $z > 3$. As a result, we analyzed 478 sGRBs with $P \geq 4.1$ photons $\text{cm}^{-2} \text{ s}^{-1}$ and $z \leq 3$.

Using the sample of 478 sGRBs with $P \geq 4.1$ photons $\text{cm}^{-2} \text{ s}^{-1}$ and $z \leq 3$, we investigated the sGRB LF and formation rate under various delay-time distribution models. We applied the maximum likelihood method to analyze the observed redshift and luminosity distributions of the sGRB sample, and used the MCMC technology to determine the best-fitting parameters for each model. We found that all delay-time distribution models seem to account for the observed redshift and luminosity distributions similarly well. Nevertheless, based on the AIC model selection criterion, the power-law delay model is slightly preferred, with an estimated relative probability of 72%. In comparison, the lognormal and Gaussian delay models are less favored, with relative probabilities of about 26% and 1%, respectively. Additionally, with the best-fitting parameters presented in Table 1, consistent local formation rates of sGRBs are obtained for different delay-time distribution models, i.e., $R_{\text{sGRB}}(0) = 1.73^{+0.60}_{-0.45} \text{ Gpc}^{-3} \text{ yr}^{-1}$ for the power-law delay model, $1.57^{+0.76}_{-0.78} \text{ Gpc}^{-3} \text{ yr}^{-1}$ for the Gaussian delay model, and $1.31^{+0.85}_{-0.61} \text{ Gpc}^{-3} \text{ yr}^{-1}$ for the lognormal delay model. These results are well-aligned with those of other works (Guetta & Piran 2005; Yonetoku et al. 2014; Ghirlanda et al. 2016; Paul 2018).

Furthermore, we explored the prospects for joint detection of sGRBs and their GW counterparts from BNS mergers using three high-energy GRB detectors (*Fermi*/GBM, *SVOM*/GRM, and *EP*/WXT) and two GW detector networks (IGWN4 and IGWN5). In our analysis, the GW detection rates by the GW detector networks were estimated using the synthetic BNS population (Bhattacharjee et al. 2024). By combining the GW detection rate with the observed sGRB distributions, we further calculated the joint sGRB and GW detection rates across various GRB and GW facilities. For the sensitivity of the IGWN4, the overall joint sGRB and GW detection rates are relatively low. Our predicted joint detection rates for the GRB detectors *Fermi*/GBM, *SVOM*/GRM, and *EP*/WXT with IGWN4 are

⁴ <https://git.ligo.org/sensitivity-curves/observing-scenario-paper-2019-2020-update/-/tree/master>

Table 2. The energy bands, flux thresholds, Sky-coverage fractions, and SAA-outage fractions of the high-energy emissions.

Mission	Energy band (keV)	Flux threshold	Sky-coverage fraction (f_{sky})	SAA-outage fraction ($f_{\text{not_SAA}}$)
<i>Fermi</i> /GBM	10–1000	4.1 (photons $\text{cm}^{-2} \text{s}^{-1}$)	0.7	0.85
<i>SVOM</i> /GRM ^(a)	1–1000	3.2 (photons $\text{cm}^{-2} \text{s}^{-1}$)	0.24	0.85
<i>EP</i> /WXT ^(b)	0.5–4	8.9×10^{-10} (erg $\text{cm}^{-2} \text{s}^{-1}$)	0.09	0.67

Note. (a) Wei et al. (2016), (b) Yuan et al. (2015).

Table 3. The sGRB and joint sGRB + GW detection rates for all combinations of high-energy GRB missions, GW networks, and delay-time distribution models. Columns 2–4 give the sGRB detection rates for the three GRB missions, independent of GW detection. Note that these rates are estimated for events with $d_L < 1.6$ Gpc (corresponding to $z < 0.3$), which is the distance limit of this work; they should not be confused with the total sGRB detection rates (see the discussion at the end of section 4.2). The last six columns provide the joint sGRB + GW detection rates. For instance, the last cell of this table states that for the power-law delay model, *EP*/WXT + IGWN5 will detect $0.20^{+0.09}_{-0.06}$ events per year. All the results are presented at the 1σ confidence level.

Delay model	sGRB detection rate (yr^{-1})			IGWN4 joint detection rate (yr^{-1})			IGWN5 joint detection rate (yr^{-1})		
	<i>Fermi</i> /GBM	<i>SVOM</i> /GRM	<i>EP</i> /WXT	<i>Fermi</i> /GBM	<i>SVOM</i> /GRM	<i>EP</i> /WXT	<i>Fermi</i> /GBM	<i>SVOM</i> /GRM	<i>EP</i> /WXT
Gaussian	$3.47^{+2.61}_{-0.88}$	$1.77^{+1.12}_{-0.84}$	$1.47^{+1.09}_{-0.72}$	$0.19^{+0.11}_{-0.09}$	$0.06^{+0.04}_{-0.03}$	$0.02^{+0.02}_{-0.01}$	$1.16^{+0.70}_{-0.56}$	$0.49^{+0.30}_{-0.23}$	$0.17^{+0.10}_{-0.08}$
Lognormal	$3.40^{+0.69}_{-1.55}$	$1.86^{+2.06}_{-0.79}$	$0.67^{+0.31}_{-0.25}$	$0.17^{+0.11}_{-0.08}$	$0.07^{+0.03}_{-0.02}$	$0.02^{+0.02}_{-0.01}$	$1.13^{+0.85}_{-0.58}$	$0.52^{+0.23}_{-0.20}$	$0.18^{+0.08}_{-0.07}$
Power law	$3.69^{+2.25}_{-1.55}$	$1.96^{+0.88}_{-0.60}$	$0.57^{+0.27}_{-0.18}$	$0.22^{+0.09}_{-0.07}$	$0.08^{+0.03}_{-0.02}$	$0.02^{+0.01}_{-0.01}$	$1.26^{+0.67}_{-0.44}$	$0.56^{+0.24}_{-0.17}$	$0.16^{+0.07}_{-0.05}$

0.09–0.31, 0.03–0.11, and 0.01–0.04 yr^{-1} , respectively, for different delay-time distribution models (see Columns 5–7 of Table 3). Our results offer a plausible explanation for the lack of joint sGRB and GW detection over a long period of observation due to the low joint detection rate of current instruments. Following the upgrade of the GW detection network to IGWN5, we expect to detect more sGRB-GW association events in the future. Specifically, with IGWN5, the joint detection rates would increase to 0.55–1.98, 0.26–0.80, and 0.09–0.27 yr^{-1} for *Fermi*/GBM, *SVOM*/GRM, and *EP*/WXT, respectively (see Columns 8–10 of Table 3).

In this research, besides *Fermi* and *SVOM*, we also studied the sGRB detection rate of *EP*. However, *EP* is specifically designed for X-ray observation, and GRB prompt emission is not the primary aim of the satellite. As expected, *EP* does not show a strong capability in the detection of sGRBs. The observed luminosity of GRB prompt emission depends on the jet structure. In all the jet structure models, the observed luminosity decreases rapidly as the angle between the line of sight and the jet increases. Most GRBs could not be detected due to off-axis observation. Differently, the afterglow of GRBs allows for observation from larger angles, and it is easier to detect in the X-ray band. However, there are insufficient sGRB afterglow samples to perform a study predicting the afterglow detection rate of an X-ray space telescope.

ACKNOWLEDGEMENTS

We are grateful to Dr. Shi-Jie Zheng, Dr. Guang-Xuan Lan, An Li, and Yi-Fang Liang for useful discussions. This work is partially supported by the Strategic Priority Research Program of the Chinese Academy of Sciences (grant No. XDB0550400), the National Key R&D Program of China (2024YFA1611704), the National Natural Science Foundation of China (grant Nos. 12422307, 12373053, and 12321003), the Key Research Program of Frontier Sciences (grant No. ZDBS-LY-7014) of Chinese Academy of Sciences, and the Natural Science Foundation of Jiangsu Province (grant No. BK20221562).

DATA AVAILABILITY

All the GRB data used in this paper can be obtained from the *Fermi* GBM catalog: <https://heasarc.gsfc.nasa.gov/W3Browse/fermi/fermigbrst.html>.

REFERENCES

- Abbott B. P., et al., 2017, *ApJ*, **848**, L13
 Abbott R., et al., 2021a, *ApJ*, **913**, L7
 Abbott R., et al., 2021b, *ApJ*, **915**, L5
 Abdo A. A., et al., 2010, *ApJ*, **720**, 435
 Acernese F., et al., 2015, *Classical and Quantum Gravity*, **32**, 024001
 Ajello M., et al., 2009, *ApJ*, **699**, 603
 Ajello M., et al., 2012, *ApJ*, **751**, 108
 Akaiki H., 1974, *IEEE Transactions on Automatic Control*, **19**, 716
 Aso Y., Michimura Y., Somiya K., Ando M., Miyakawa O., Sekiguchi T., Tatsumi D., Yamamoto H., 2013, *Phys. Rev. D*, **88**, 043007
 Atteia J. L., Cordier B., Wei J., 2022, *International Journal of Modern Physics D*, **31**, 2230008
 Babak S., Hewitson M., Petiteau A., 2021, *arXiv e-prints*, p. arXiv:2108.01167
 Band D., et al., 1993, *ApJ*, **413**, 281
 Barsotti L., McCuller L., Evans M., Fritschel P., 2018, The A+ design curve, <https://dcc.ligo.org/LIGO-T1800042-v4/public>
 Beniamini P., Granot J., Gill R., 2020a, *MNRAS*, **493**, 3521
 Beniamini P., Duran R. B., Petropoulou M., Giannios D., 2020b, *ApJ*, **895**, L33
 Berger E., 2014, *ARA&A*, **52**, 43
 Bhattacharjee S., et al., 2024, *MNRAS*, **528**, 4255
 Burns E., 2020, *Living Reviews in Relativity*, **23**, 4
 Chiang J., Mukherjee R., 1998, *ApJ*, **496**, 752
 Dainotti M. G., Petrosian V., Bowden L., 2021, *ApJ*, **914**, L40
 Dietz A., 2011, *A&A*, **529**, A97
 Dimitrova T. A., Butler N. R., Ravi S., 2023, *ApJ*, **949**, 15
 Eichler D., Livio M., Piran T., Schramm D. N., 1989, *Nature*, **340**, 126
 Faber J. A., Rasio F. A., 2012, *Living Reviews in Relativity*, **15**, 8
 Foreman-Mackey D., Hogg D. W., Lang D., Goodman J., 2013, *PASP*, **125**, 306

- Ghirlanda G., et al., 2016, *A&A*, **594**, A84
- Ghirlanda G., et al., 2019, *Science*, **363**, 968
- Goldstein A., et al., 2017, *ApJ*, **846**, L5
- Gruber D., et al., 2014, *ApJS*, **211**, 12
- Guetta D., Piran T., 2005, *A&A*, **435**, 421
- Guetta D., Piran T., 2006, *A&A*, **453**, 823
- Guetta D., Stella L., 2009, *A&A*, **498**, 329
- Hannam M., Schmidt P., Bohé A., Haegel L., Husa S., Ohme F., Pratten G., Pürrer M., 2014, *Phys. Rev. Lett.*, **113**, 151101
- Hinshaw G., et al., 2013, *ApJS*, **208**, 19
- Iyer B., Souradeep T., Unnikrishnan C., Dhurandhar S., Raja S., Sengupta A., 2011, LIGO-India, Proposal of the Consortium for Indian Initiative in Gravitational-wave Observations (IndIGO), <https://dcc.ligo.org/LIGO-M1100296/public>
- Kaneko Y., Preece R. D., Briggs M. S., Paciesas W. S., Meegan C. A., Band D. L., 2006, *ApJS*, **166**, 298
- Khan S., Husa S., Hannam M., Ohme F., Pürrer M., Forteza X. J., Bohé A., 2016, *Phys. Rev. D*, **93**, 044007
- Kouveliotou C., Meegan C. A., Fishman G. J., Bhat N. P., Briggs M. S., Koshut T. M., Paciesas W. S., Pendleton G. N., 1993, *ApJ*, **413**, L101
- LIGO Scientific Collaboration et al., 2015, *Classical and Quantum Gravity*, **32**, 074001
- Lan G.-X., Zeng H.-D., Wei J.-J., Wu X.-F., 2019, *MNRAS*, **488**, 4607
- Lan G.-X., Wei J.-J., Zeng H.-D., Li Y., Wu X.-F., 2021, *MNRAS*, **508**, 52
- Lan G.-X., Wei J.-J., Li Y., Zeng H.-D., Wu X.-F., 2022, *ApJ*, **938**, 129
- Liddle A. R., 2007, *MNRAS*, **377**, L74
- Liu H.-Y., Yu Y.-W., 2019, *Research in Astronomy and Astrophysics*, **19**, 118
- Luo J.-W., Li Y., Ai S., Gao H., Zhang B., 2022, *MNRAS*, **516**, 1654
- Lyman J. D., et al., 2018, *Nature Astronomy*, **2**, 751
- Lynden-Bell D., 1971, *MNRAS*, **155**, 95
- Margutti R., et al., 2018, *ApJ*, **856**, L18
- Marshall H. L., Tananbaum H., Avni Y., Zamorani G., 1983, *ApJ*, **269**, 35
- Mooley K. P., et al., 2018a, *Nature*, **561**, 355
- Mooley K. P., et al., 2018b, *ApJ*, **868**, L11
- Nakar E., 2007, *Phys. Rep.*, **442**, 166
- Nakar E., 2020, *Phys. Rep.*, **886**, 1
- Nakar E., Gal-Yam A., Fox D. B., 2006a, *ApJ*, **650**, 281
- Nakar E., Gal-Yam A., Fox D. B., 2006b, *ApJ*, **650**, 281
- Narayana Bhat P., et al., 2016, *ApJS*, **223**, 28
- Narumoto T., Totani T., 2006, *ApJ*, **643**, 81
- Özel F., Freire P., 2016, *ARA&A*, **54**, 401
- Pai A., Dhurandhar S., Bose S., 2001, *Phys. Rev. D*, **64**, 042004
- Paul D., 2018, *MNRAS*, **477**, 4275
- Petrillo C. E., Dietz A., Cavaglià M., 2013, *ApJ*, **767**, 140
- Petrov P., et al., 2022, *ApJ*, **924**, 54
- Preece R. D., Briggs M. S., Mallozzi R. S., Pendleton G. N., Paciesas W. S., Band D. L., 2000, *ApJS*, **126**, 19
- Saleem M., et al., 2022, *Classical and Quantum Gravity*, **39**, 025004
- Savchenko V., et al., 2017, *ApJ*, **848**, L15
- Schmidt P., Hannam M., Husa S., 2012, *Phys. Rev. D*, **86**, 104063
- Siellez K., Boër M., Gendre B., 2014, *MNRAS*, **437**, 649
- Sun H., Zhang B., Li Z., 2015, *ApJ*, **812**, 33
- Tan W.-W., Fan X.-L., Wang F. Y., 2018, *MNRAS*, **475**, 1331
- Troja E., et al., 2017, *Nature*, **551**, 71
- Troja E., et al., 2018, *Nature Communications*, **9**, 4089
- Troja E., et al., 2020, *MNRAS*, **498**, 5643
- Tsutsui R., Yonetoku D., Nakamura T., Takahashi K., Morihara Y., 2013, *MNRAS*, **431**, 1398
- Virgili F. J., Zhang B., O'Brien P., Troja E., 2011, *The Astrophysical Journal*, **727**, 109
- Wanderman D., Piran T., 2015, *Monthly Notices of the Royal Astronomical Society*, **448**, 3026
- Wei J., et al., 2016, *arXiv e-prints*, p. [arXiv:1610.06892](https://arxiv.org/abs/1610.06892)
- Woosley S. E., 1993, *ApJ*, **405**, 273
- Yonetoku D., Murakami T., Nakamura T., Yamazaki R., Inoue A. K., Ioka K., 2004, *ApJ*, **609**, 935
- Yonetoku D., Nakamura T., Sawano T., Takahashi K., Toyonago A., 2014, *ApJ*, **789**, 65
- Yuan W., et al., 2015, *arXiv e-prints*, p. [arXiv:1506.07735](https://arxiv.org/abs/1506.07735)
- Yuan W., Zhang C., Chen Y., Ling Z., 2022, in Bambi C., Sanganello A., eds., *Handbook of X-ray and Gamma-ray Astrophysics*. p. 86, [doi:10.1007/978-981-16-4544-0_151-1](https://doi.org/10.1007/978-981-16-4544-0_151-1)
- Yüksel H., Kistler M. D., Beacom J. F., Hopkins A. M., 2008, *ApJ*, **683**, L5
- Zhang G. Q., Wang F. Y., 2018, *ApJ*, **852**, 1
- Zhu X., Thrane E., Osłowski S., Levin Y., Lasky P. D., 2018, *Phys. Rev. D*, **98**, 043002
- von Kienlin A., et al., 2014, *ApJS*, **211**, 13
- von Kienlin A., et al., 2020, *ApJ*, **893**, 46

This paper has been typeset from a $\text{\TeX}/\text{\LaTeX}$ file prepared by the author.